ASIA TURBOMACHINERY & PUMP SYMPOSIUM
23-26 FEBRUARY 2021
SHORT COURSES: 22 FEBRUARY 2021

MEASURED LEAKAGE AND ROTORDYNAMIC-COEFFICIENTS FOR THE FOLLOWING LIQUID ANNULAR SEALS: (A) SMOOTH-ROTOR/GROOVED-STATOR, AND (B) GROOVED-ROTOR/SMOOTH-STATOR

Dara W. Childs
Professor Emeritus
J. Mike Walker '66 Department of Mechanical Engineering
Texas A&M University
College Station, TX
dchilds@tamu.edu

Jing Yang
Assistant Research Engineer
J. Mike Walker '66 Department of Mechanical Engineering
Texas A&M University
College Station, TX
yangjing@tamu.edu

Jose M. Torres Rueda
Senior Mechanical Engineer
Energy Recovery, Inc.
Katy, TX
joset91@gmail.com

J. Alex Moreland
Engineering Specialist
Lynntech, Inc.
College Station, TX
morelandjames9292@gmail.com

Luis San Andrés
Mast-Childs Chair Professor
J. Mike Walker '66 Department of Mechanical Engineering
Texas A&M University
College Station, TX
lsanandres@tamu.edu

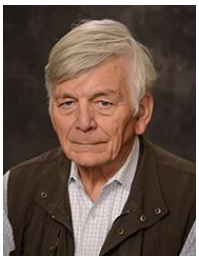

Dara W. Childs, P.E. was Director of the Turbomachinery Laboratory from 1984 to 2018 and held the Leland T. Jordan Chair in Mechanical Engineering at Texas A&M University. He received B.S. and M.S. degrees (Civil Engineering, 1961, 1962) from Oklahoma State University, and his Ph.D. (Engineering Mechanics, 1968) from the University of Texas. He was named ASME Fellow Member in 1990 and received ASMEs Henry R. Worthington Medal in 1991, and GPPS 2019 Lifetime Achievement Award. Dr. Childs' expertise is in dynamics and vibrations, with an emphasis in rotordynamics. He has conducted research and engineering projects for NASA, DOD, and private firms. Current research includes high-pressure testing honeycomb and hole-pattern gas damper seals; testing high-pressure laminar oil seals; force measurements in magnetic bearings using fiber-optic strain gauges. Dr. Childs has authored numerous reviewed publications related to rotordynamics and vibrations, and the books, Turbomachinery Rotordynamics, and Turbomachinery Rotordynamics with Case Studies, etc.

Jing Yang received her B.S. in Thermal and Power Engineering from Huazhong University of Science and Technology, China in 2010 and Ph.D. degree in Fluid Mechanics from Peking University, China in 2017. After graduation in 2016, she worked for three years as a post-doctoral Research Associate at the TEES Turbomachinery Laboratory. Since October 2019, Jing continues at the Turbo Lab as an Assistant Research Engineer. Jing Yang's research mainly focuses on the numerical prediction (computational fluid dynamics and bulk flow model) and experimental verification of the dynamic forced performance of annular pressure seals and fluid film bearings.

Jose developed an affinity for airplanes as a young boy. In 2008, eight years after moving to Miami, Florida, he decided to pursue his interest, and launched into University of Florida's Aerospace Engineering program. During his undergrad career, Jose completed 4 internships with GE Aviation on the areas of Rotordynamics, Compressor Design, Facilities, and Manufacturing. This exposure introduced him to the wonders of turbomachinery, and motivated him to explore them in the Energy Sector. After completing two Machinery Engineer Internships at ExxonMobil, Jose went back to Academia to obtain a Mechanical Engineering M.S. focused on Rotordynamics, at Texas A&M. He later worked for 3.5 years as Exxon's Gulf of Mexico's Machinery Engineer, optimizing production via machinery upgrades, and increasing integrity through robust maintenance

programs. In 2018, Jose decided to apply his skills as a Sr. Mechanical Engineer in Energy Recovery's Research and Development department, where he led the design and implementation of the Department's first Design Process program. Drawn to the managerial side of Engineering, Jose now works as the Program Manager for Energy Recovery's next-generation technologies. In his free time, Jose enjoys playing beach Volleyball, Soccer, DJing, and spending time with Family.

Alex Moreland is currently an engineer at Lynntech, Inc., a small business in College Station, TX focused on developing new technologies and products for government-sponsored initiatives and the commercial marketplace through the SBIR program. Prior to his time at Lynntech, he worked at the Texas A&M Turbomachinery Laboratory as a graduate student characterizing liquid annular seals for applications in electrical submersible pumps. He received his B.S. in Mechanical Engineering from the University of Missouri in 2013 and his M.S. in Mechanical Engineering from Texas A&M University in 2016.

Luis San Andrés performs research in lubrication and rotordynamics, having produced advanced technologies of hydrostatic bearings for primary power cryogenic turbo pumps, squeeze film dampers for aircraft jet engines, and gas foil bearings for oil-free micro turbomachinery. Luis is a Fellow of ASME and STLE, and a member of the Industrial Advisory Committees for the Texas A&M Turbomachinery Symposia. Dr. San Andrés has educated dozens of graduate students serving the profession. Dr. San Andrés earned a MS in ME from the University of Pittsburgh and a PhD in ME from Texas A&M University. Luis has published over 250 peer reviewed papers in numerous ASME *journals and conferences, including* TPS and ATPS. *Several papers are recognized as best in various international conferences.*

ABSTRACT

Test results are presented and compared for the following annular pump seal geometries: (a) a smooth-rotor/circumferentially-grooved stator (SR/GS) and (b) a smooth-stator/circumferentially-grooved rotor (GR/SS). The GR/SS seal's geometry and operating conditions are representative of electrical submersible pumps (ESPs) as used for oil recovery. The SR/GS seals' nominal dimensions are identical with the GR/SS seal except for the reversed groove locations. Test results include static and rotordynamic data at speeds ω of 2, 4, 6 krpm for the SR/GS and 2, 4, 6, 8 krpm for the GR/SS seal. Both seals have axial pressure drops ΔP of 2.1, 4.1, 6.2, 8.3 bars, a length-to-diameter ratio L/D of 0.5, and a minimum radial clearance C_r of 203 μm. They employ 15 circumferential grooves with a length G_l, and depth G_d of 1.52 mm, which are equally spaced with a land length of 1.52 mm. Results are presented for centered conditions. Three different inlet-fluid pre-rotation inserts are used upstream of the test seals to create a range of inlet preswirl ratios. A Pitot tube is used to measure the circumferential velocity at one location immediately upstream of the test seals. The test fluid is ISOVG2 oil @ 46 °C.

The GR/SS seal leaks about 10% more than the SR/GS seal. Generally, direct stiffness (K_{xx}, K_{yy}) values for both designs have low magnitudes that drop with increasing ω. The GR/SS seals' K_{xx}, K_{yy} values dropped more rapidly and were negative at 6 krpm. For the SR/GS seals, K_{yy} was negative at 6 krpm, but K_{xx} was still positive. With either design, instability issues are as likely to arise because of negative direct stiffness that pulls down a pump's critical speed versus directly destabilizing K_{xy}, K_{yx} coefficients. In the same operating conditions, the K_{xy}, K_{yx} coefficients' magnitudes are ~2.5 times larger for GR/SS seals than for SR/GS seals --- significantly more destabilizing. Under the same conditions, the SR/GS seal has slightly more direct damping than the GR/SS seal. Direct virtual mass coefficients are about 20% larger for the SR/GS seals, inducing a lower critical speed.

Whirl frequency ratio (WFR) combines the effects of the cross-coupled stiffness, direct damping, and cross-coupled mass terms and provides the best measure for comparing the two seal designs' stability characteristics. Overall, the GR/SS seal WFR values are about three times higher than the comparable values for SR/GS seals --- much less stable. Effective swirl brakes that could sharply drop the seals' inlet preswirl would be helpful for the GR/SS seal out to 4 krpm and helpful for the SR/GS seal out to 6 krpm.

INTRODUCTION

Smooth annular liquid seals have typical radial clearance C_r to shaft radius R ratios (C_r/R) of 0.002 and develop reaction forces via the hydrodynamic (fluid rotation) effect, and the Lomakin effect [1]. Rotordynamic coefficients are used to model a seal's reaction-force components f_{sx}, f_{sy} for small perturbations about an equilibrium position in the following reaction-force model:

$$-\begin{Bmatrix} f_{sx} \\ f_{sy} \end{Bmatrix} = \begin{bmatrix} K_{xx} & K_{xy} \\ K_{yx} & K_{yy} \end{bmatrix} \begin{Bmatrix} \Delta x \\ \Delta y \end{Bmatrix} + \begin{bmatrix} C_{xx} & C_{xy} \\ C_{yx} & C_{yy} \end{bmatrix} \begin{Bmatrix} \Delta \dot{x} \\ \Delta \dot{y} \end{Bmatrix} + \begin{bmatrix} M_{xx} M_{xy} \\ M_{yx} M_{yy} \end{bmatrix} \begin{Bmatrix} \Delta \ddot{x} \\ \Delta \ddot{y} \end{Bmatrix} \quad (1)$$

where $\Delta x, \Delta y$ are the relative displacement components between the seal stator and the shaft. Also, the K_{ij},C_{ij}, and M_{ij} coefficients are a function of ϵ_0 the seal eccentricity ratio. For small motion about a centered position, the eccentricity-dependent model of Eq. (1) can be replaced by the following simplified reaction-force model:

$$-\begin{Bmatrix} f_{sx} \\ f_{sy} \end{Bmatrix} = -\begin{bmatrix} K & k \\ -k & K \end{bmatrix}\begin{Bmatrix} \Delta x \\ \Delta y \end{Bmatrix} - \begin{bmatrix} C & c \\ -c & C \end{bmatrix}\begin{Bmatrix} \Delta \dot{x} \\ \Delta \dot{y} \end{Bmatrix} - \begin{bmatrix} M & m \\ -m & M \end{bmatrix}\begin{Bmatrix} \Delta \ddot{x} \\ \Delta \ddot{y} \end{Bmatrix} \tag{2}$$

where $K = K_{xx} = K_{yy}$, $k = K_{xy} = -K_{yx}$, $C = C_{xx} = C_{yy}$, $c = C_{xy} = -C_{yx}$, $M = M_{xx} = M_{yy}$, $m = M_{xy} = -M_{yx}$.

Test results have shown that the models of Eqs. (1-2) generally also apply for grooved annular seals.

Various "bulk-flow" models have been developed to predict the static (leakage) and rotordynamic characteristics for circumferentially grooved seals. Recently, CFD methods [2] have also been applied to predict the behavior of these seal types. The present paper presents test data only (no comparisons to predictions) for two circumferentially grooved seals that are identical except for the groove location. Prior test results are only discussed for grooved seals --- no smooth seals.

In 1990, Florjancic and McCloskey [3] presented test results for a centered, smooth-rotor/circumferentially-grooved-stator (SR/GS) seal. Their test rig generated a low pre-swirl ratio

$$PSR = \frac{v_{inlet}}{\omega R} \tag{3}$$

on the order of 0.25 where v_{inlet} is the average circumferential velocity measured upstream from the seal and ω is shaft running speed. Differential pressures (ΔPs) reached 60 bars.

From Eq. (2), for synchronous precession, effective stiffness is

$$K_{eff} = -K + C\omega - M\omega^2 \tag{4}$$

It is the net centering stiffness for small motion about a centered position. Similarly, effective damping is

$$C_{eff} = C - \frac{k}{\omega} + m\omega \tag{5}$$

It defines the net damping coefficient for small motion about the center of a seal.

In 1990, Kilgore and Childs [4] measured K_{eff}, C_{eff} for six SR/GS liquid-seals. They varied ω from 1 to 7.2 krpm, and ΔP from 2.5 to 27.5 bar, creating turbulent-flow conditions. Their test rotors were centered. Upstream flow was injected radially from two opposed inlet ports.

In 1997, Marquette et al. [5] used a "shake-the-stator" rig whose concept was first introduced by Glenicke [6] for hydrodynamic bearings. They measured leakage and rotordynamic performance of SR/GS seals while varying ΔP from 41 to 64 bars, ω from 10.2 to 24.6 krpm, and ϵ_0 from 0.00 to 0.50. When compared to smooth seals, they concluded that the grooves provide an increase in sealing capacity at the cost of reduced and even negative *K* values. They used nominally radial injection of flow upstream of the seal and did not measure circumferential velocity upstream of the test seals.

In 2018, Moreland et al. [7] and Childs et al. [8] presented test data, respectively, for annular pump seals with: (a) a GR/SS seal, and (b) a SR/GS seal. The SR/GS and GR/SS seals were identical except for the flipped groove locations. Moreland et al.'s paper [7] used data from Moreland's thesis [9], while Childs et al. [8] used data from Torres-Rueda's thesis [10]. They used the same test rig used in here and compared their measured results to results for a smooth seal with the same *L, D* and minimum C_r values. In all cases, rotordynamic coefficients for the smooth seal were much larger than corresponding results for grooved seals. In the present paper, data from [9] and [10] are used to directly compare the leakage and rotordynamic characteristics of the SR/GS and GR/SS seals. The GR/SS seal's geometry and operating conditions are representative of an interstage seal for an electrical submersible pumps (ESPs) as used for oil recovery. Figure 1 provides a cross-section of an ESP.

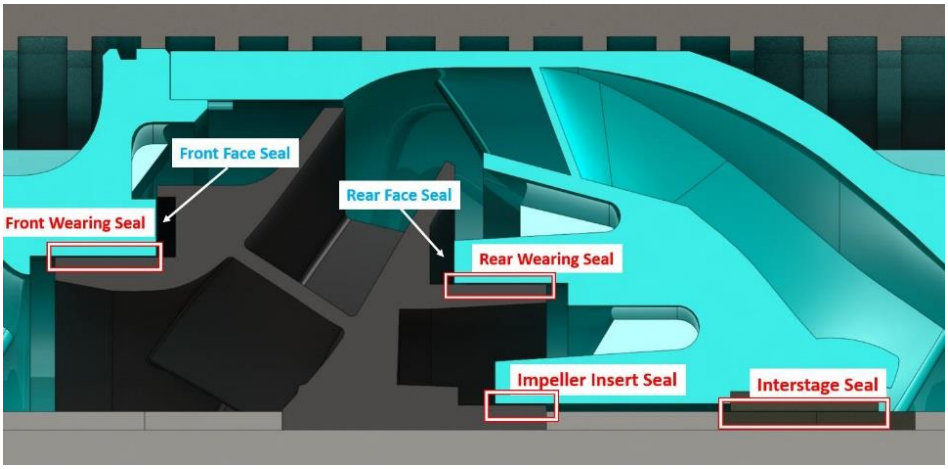

Figure 1. ESP cross section [11].

STATEMENT OF WORK

Test Seal Geometry

Figure 2 shows the test seals featuring 15 equally-spaced grooves, each 1.52 mm deep, with entrance and exit land lengths of 3.30 mm, and a minimum radial clearance C_r of .203 mm.

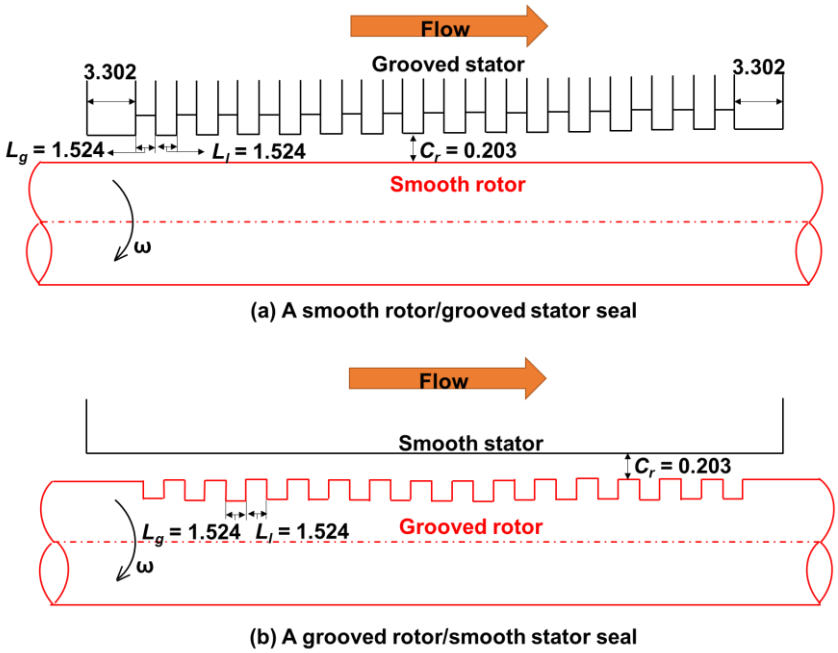

Figure 2. Two grooved seals geometry and grooves details. All dimensions are in mm; rotor diameter *D* = 101.6 mm. Design clearances are shown.

Test Matrix

Three different inlet preswirl rings are used to create a range of preswirl ratio(PSR) values. For each preswirl ring, tests are conducted for ΔP = 2.07, 4.14, 6.21, and 8.27 bars. The GR/SS seal was tested at ω = 2, 4, and 6 krpm; the SR/GS seal was tested at ω = 2, 4, 6, and 8 krpm.

TEST RIG DESCRIPTION

Test Rig

The test rig was initially designed to determine leakage and rotordynamic properties of compressor oil bushing seals by Kaul in 1999 [12]. Kleutinberg [13] describes the rig's configuration, hardware, and operational procedures for testing fluid-film bearings. Moreland et al. [7] and Moreland [9] describe the modifications of the test rig in converting from testing hydrodynamic bearings to annular seals.

Figure 3 shows the test rig's main elements: the driver, the coupling, the shaft, the shaker system, the pedestal, and the test section. The driver is a VFD-controlled electric motor that can reach 8 krpm.

Supported by angular-contact hybrid ceramic ball bearings, the AISI 4041 steel shaft attaches to the electric motor via a disk-pack hybrid coupling and a hydraulic hub. The shaft was precision machined to a diameter of 101.600 mm at the test-seal film lands and uses six pitch stabilizers to achieve axial alignment with respect to the seal. The hybrid ceramic bearings are mist lubricated.

Figure 4 is a close-up view of the main rotor-assembly components. Oil enters through two ports placed 180° from each other and then accelerates thought preswirl-insert nozzles to achieve a range of inlet circumferential velocities before reaching the seal inlet. After flowing through the test seals, the oil accumulates in the cavity between the seal holder and rotor, finally exiting the test section through collection chambers at near-atmospheric pressure.

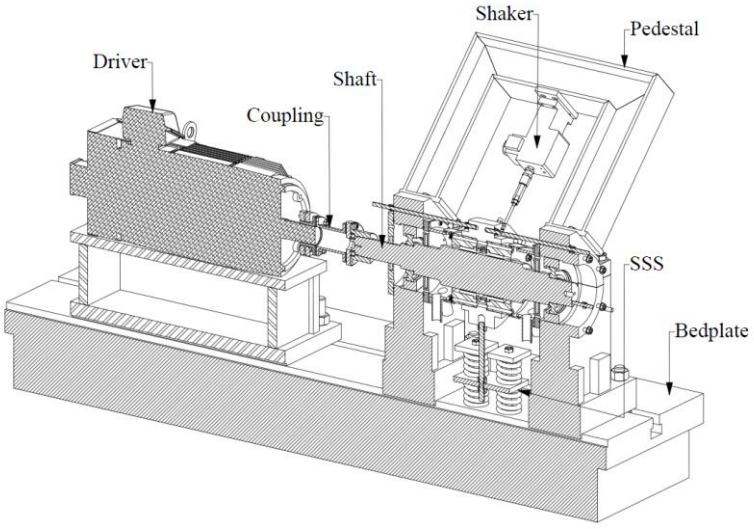

Figure 3. Main test rig components [8].

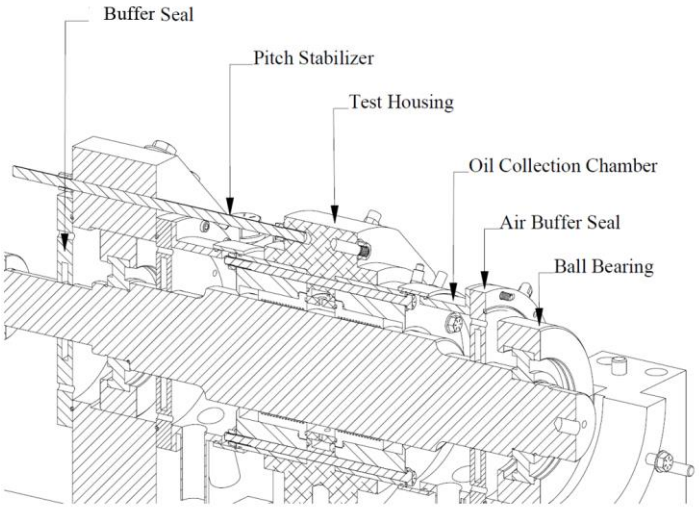

Figure 4. Main rotor-assembly components [8].

Instrumentation

Figure 5 shows that the test section stator houses the grooved-seal elements, accommodates most of the instrumentation, and accepts connections for the oil inlet, static loader, and dynamic shaker heads. Also shown in Fig. 5 is the instrumentation used to measure and record the test variables.

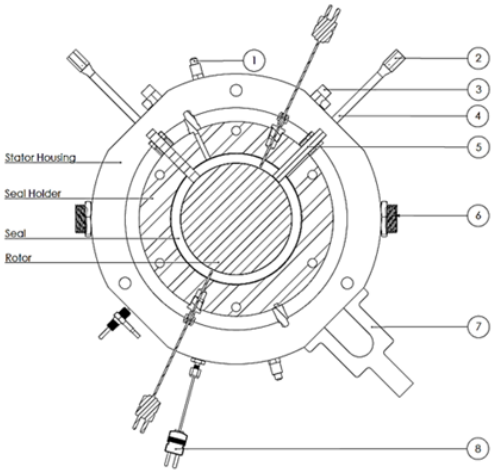

Item	Description
1	Pressure Probe
2	Load Cell
3	Accelerometer
4	Dynamic Shaker
5	Proximity Probe
6	Oil Inlet
7	Static Loader
8	Thermocouple

Figure 5. Test section assembly with main instrumentation [8].

Pre-Swirl Inserts

The pre-swirl-inserts shown in Fig. 6 were designed to achieve low, medium, and high circumferential fluid velocity at the seal inlet.

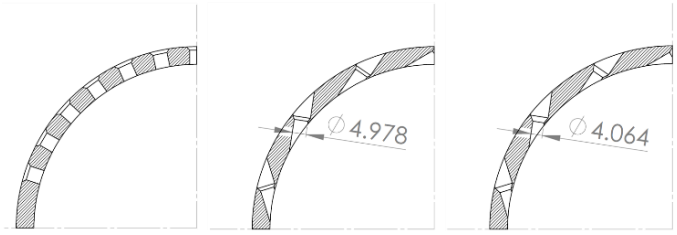

Figure 6. Cross-section view of (a) radial injection (low PSR), (b) tangential injection (medium PSR), and (c) tangential injection (high PSR) inserts. (Unit: mm) [7].

Spring stabilization system (SSS)

The test seals had low and sometimes negative direct stiffness values that dropped the test stator's natural frequency, initially causing excessive stator subsynchronous vibration for ω > 4 krpm. Consequently, the set of vertical and diagonal springs shown in Fig. 7 were attached to the stator housing, increasing the stator's support stiffness and allowing higher running speeds.

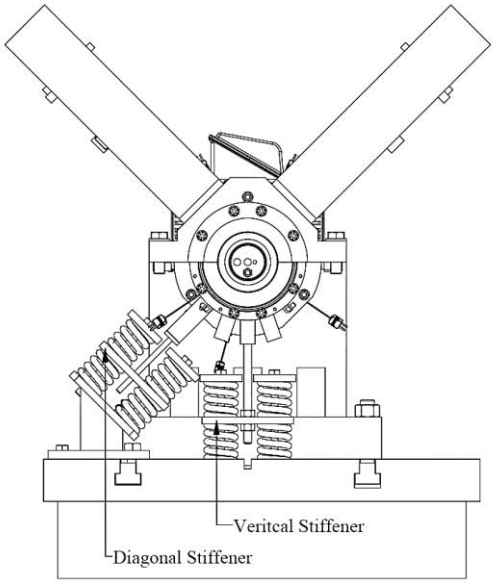

Figure 7. Non-Drive End (NDE) view showing the added vertical and diagonal stiffeners [8].

STATIC RESULTS

Seal eccentric location and coordinate system

The seals were tested over the eccentricity-ratio range: 0.00, 0.27, 0.53, and 0.80. The rotordynamic coefficients are only slightly affected by changes in ϵ_0; hence, only centered results are shown here.

Figure 8 shows the *x*-*y* coordinate system with the static load applied in the $-y$ direction. Note that ϵ_0=0.0 corresponds to a perfectly centered seal, and ϵ_0 =1.0 implies shaft contact.

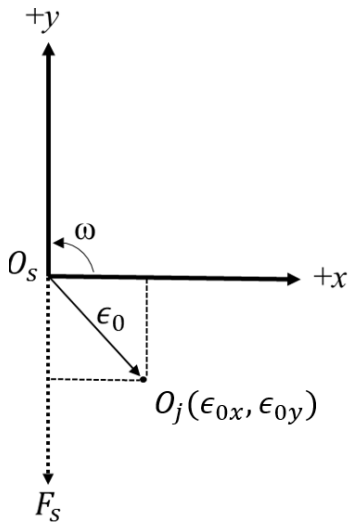

Figure 8. Coordinate system [8].

Measuring Hot Clearances

Gently pushing the stator around the seal yields a clearance circle as recorded by the proximity probes. The clearances reported below are "hot" clearances, recorded after a speedy shutdown once the flow loop has reached thermal equilibrium. For the SR/GS seal [10], the radial clearances are 183.9, 190.67, and 190.43 µm, respectively, for the low, medium, and high preswirl inserts. For the GR/SS seal, the radial clearances are 183.81, 185.62, and 187.12 µm, respectively, for the low, medium, and high preswirl inserts [9].

Leakage

Figure 9 shows $\dot{Q}$ markedly increasing with increasing ΔP and modestly decreasing with increasing ω. In all cases, the SR/GS seal leaks more than the GR/SS seal; however, note that C_r = 183.9 µm for the SR/GS seal versus 183.81 for the GR/SS seal. The closeness of these C_r values indicates that the leakage-rate differential shown in Fig. 9 is correctly representative of the two seal designs. The drive motor has a top speed of 8 krpm. However, stator instabilities limited the SR/GS top test speeds, despite the stiffening springs shown in Fig. 7.

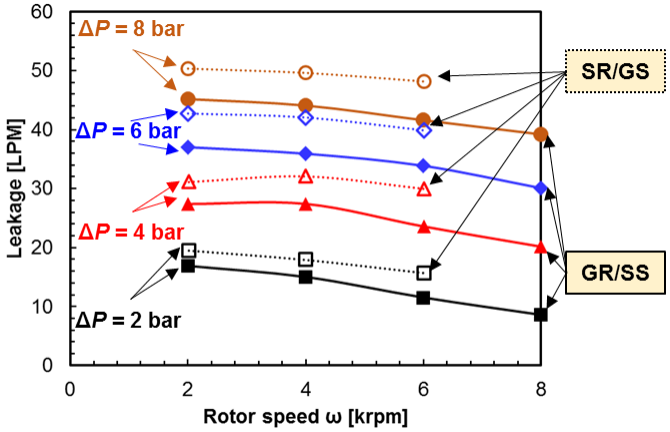

Figure 9. Measured $\dot{Q}$ versus ω for the SR/GS and GR/SS seals. ΔP = 2, 4, 6, 8 bar; low PSR.

Reynolds Number

For the grooved seal, the maximum clearance C_{max} between the rotor and the seal is

$$C_{max} = C_r + G_d \tag{6}$$

It is used to define the circumferential and axial Reynolds number, respectively as

$$Re_\theta = \rho R \omega C_{max}/\mu \tag{7}$$

$$Re_z = 2\rho\, w C_{max}/\mu \tag{8}$$

In Eq. (8), w represents the bulk-flow axial fluid velocity defined as

$$w = \dot{Q}/A \tag{9}$$

where A is the annulus flow area. The net Reynolds number is

$$Re = \sqrt{Re_\theta^2 + Re_z^2} \tag{10}$$

Full Reynolds-number results for the grooved seal are provided in [9, 10]. All flow is well within the turbulent regime.

Upstream and Downstream Circumferential Fluid Velocity

Figure 10 shows locations upstream and downstream of the seal where Pitot tubes are installed to measure circumferential velocity. Using custom gage blocks, the Pitot tubes are aligned to point in the shaft's circumferential direction. With the Pitot tube differential pressure, $\Delta \boldsymbol{P_v}$, and the fluid density, the circumferential velocity is:

$$v = \sqrt{\frac{2\Delta P_v}{\rho}} \tag{11}$$

Equation (3) defined the preswirl ratio. The outlet preswirl ratio is defined similarly and is provided in [7-10] but is not repeated here. For the low PSR insert, Figs. 11(a) and 11(b) show the GR/SS and SR/GS seal's PSR values versus ω for a range of ΔP values. PSR rises steadily with increasing ω, which is counter intuitive, given that PSR = $v_{inlet}/R\,\omega$. The authors have no explanation for this outcome. To the extent that measured PSR arises due to shaft rotation, the drop in PSR with increasing ΔP in regard to Fig. 11(b) could be explained by a reduced time exposure to accelerating shaft shear forces with lower ΔP.

For the high PSR insert, Figs. 11(c) and 11(d) show the GR/SS and SR/GS seal's PSR values versus ω for a range of ΔP values. With the exception of the ΔP= 2 bar case in Fig. 11(c), these results conform to expectations; specifically PSR increases with increasing ΔP and drops with increasing speed. Generally, for the same values of ω and ΔP, PSR is higher for the SR/GS seal than for the GR/SS seal. Also, PSR is (as expected) consistently higher for the low preswrirl insert of Fig. 10a and 10b than for the high preswirl insert of Figs. 11(c) and 11(d).

Note test results are presented for the SR/GS seal over the ω range of [2-8 krpm] but only over [2-6 krpm] for the GR/SS seal because of differing stator-instability characteristics of the separate configurations.

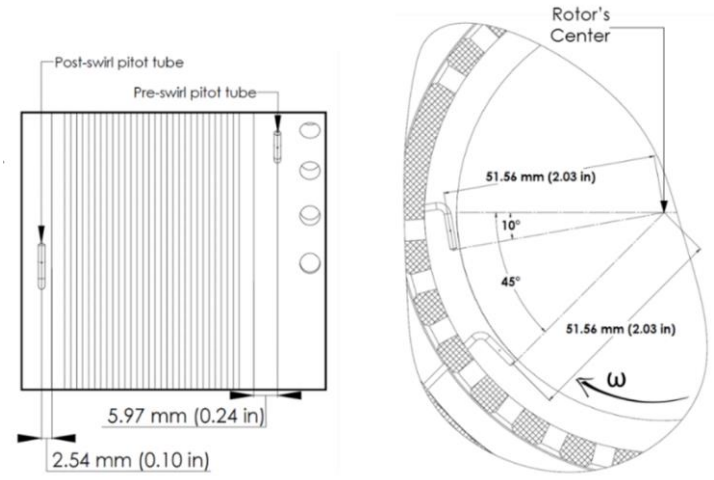

Figure 10. Pitot tubes. (a) Stator housing cross-section. (b) Pitot tube axial positions upstream and downstream of a test seal [8].

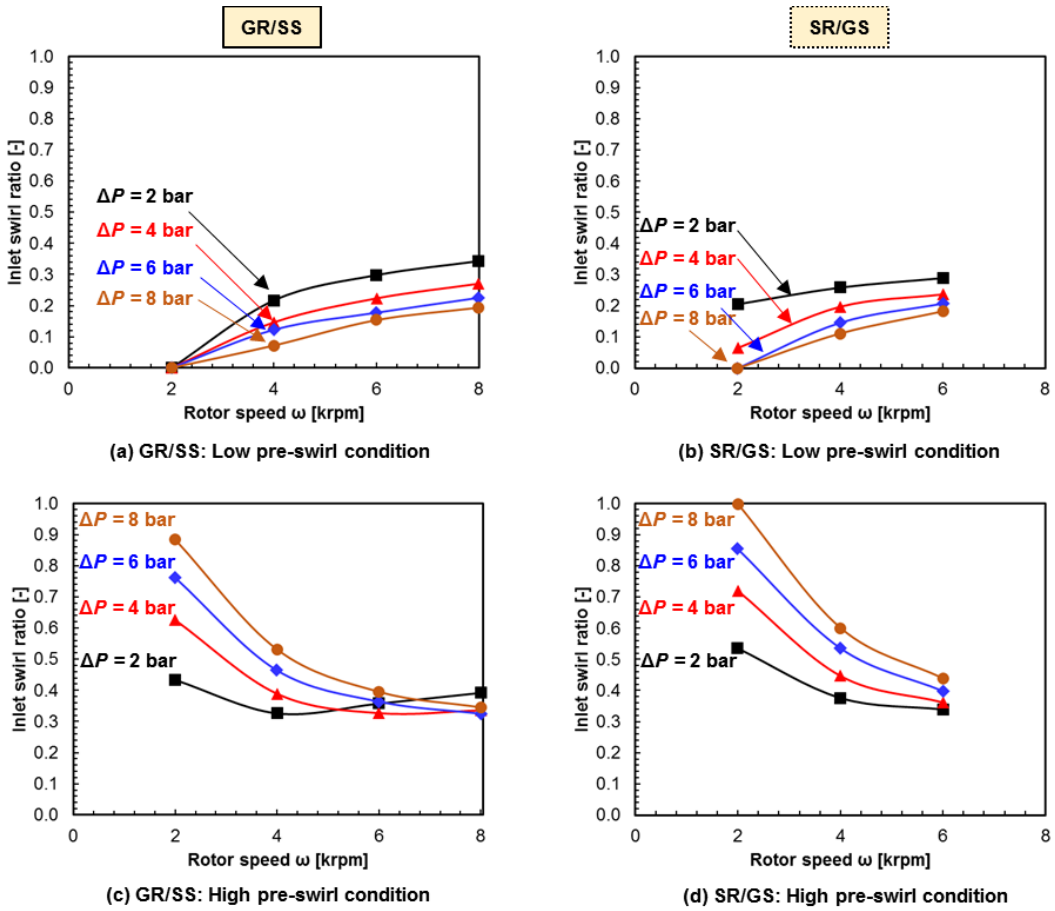

Figure 11. PSR versus ω over the ΔP range for the two grooved seals for low and high PSR-insert configurations.

MEASURING SEAL DYNAMIC STIFFNESS COEFFICIENTS

Test Procedure

To determine the stator assembly dynamics (alone), the operator applies dynamic excitations to the stator at zero speed without lubricant in the system. These "dry shake" baselines are subtracted from measurements with oil to provide only the seal's fluid-film dynamic stiffness. The operator adjusts ω, $\dot{Q}$, and static load to achieve the target test conditions. After reaching stable steady-state operation, the hydraulic shakers are used to perturb the stator assembly with a multi-frequency, pseudo-random waveform detailed by Rouvas and Childs [14]. The waveform contains frequencies ranging from approximately 10-350 Hz at intervals of 9.765 Hz. There are two separate shakes for each test point in the orthogonal direction (x, y) shown in Fig. 8.

Parameter Identification

Childs and Hale [15] detail the procedure for calculating dynamic stiffness from measured excitation forces, stator accelerations, and relative stator-rotor displacements. The dynamic-stiffness coefficient has the form

$$\boldsymbol{H_{ij}} = \left(K_{ij} - \Omega^2 M_{ij}\right) + \boldsymbol{j}(\Omega C_{ij}) \tag{12}$$

where Ω is the excitation frequency. After the baselines have been subtracted, the dynamic stiffness values are separated into the real and imaginary components. Least-squares regression curve fits are applied to the real and imaginary parts of the dynamic stiffness values. The coefficients from these curve fits are the K_{ij}, C_{ij}, and M_{ij} values of Eq.(12). The curve fit excitation frequencies extended out to 200 Hz, twice the maximum running speed of 6 krpm (100 Hz). The least-squares regression analysis as detailed by Rouvas and Childs [14] was employed. A 95% confidence interval is used for repeatability calculations. A statistical test described in Ref. [17] is used to calculate confidence intervals for the rotordynamic coefficients.

K_{xx}, K_{yy} Coefficients

For the low PSR insert, the frames of Fig. 12 shows K_{xx}, K_{yy} versus ω over a range of ΔP values for both seal configurations. As the results are for a nominally centered location, one would expect K_{xx} and K_{yy} to be approximately equal but they obviously are not. The

authors have no explanation for this outcome. The hydraulic shakers could be used in either a load-control or position-control mode. Smooth seal would "self center" in the absence of an applied external load and could be tested in the load-control mode. By contrast, in most unloaded cases, the grooved seals would not remain centered. Hence, the present test results were obtained using position control producing a "nominally" centered positon.

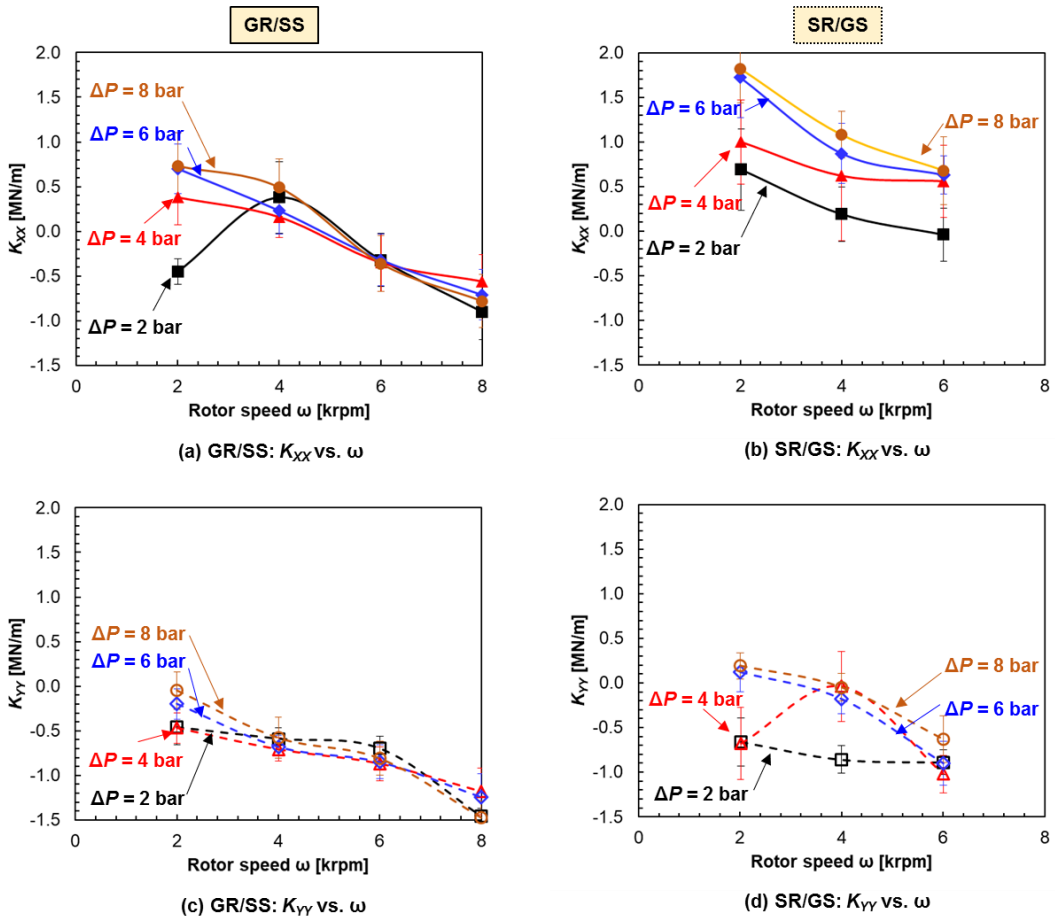

Figure 12. low inlet pre-swirl ratio. K_{XX} and K_{YY} versus ω [krpm]. ΔP = 2, 4, 6, 8 bar; ω = 2, 4, 6, 8 krpm.

For the GR/SS seal, Fig. 12(a), shows K_{xx} generally dropping with increasing ω transitioning from positive to negative. The ΔP = 2 bar result differs in first climbing as ω increases from 2 to 4 bars. At ω = 2 krpm, K_{xx} increases steadily with increasing ΔP. At higher speeds, K_{xx} values tend to converge independently of ΔP variations. Figure 12(b) shows K_{xx} for the SR/GS seal to be generally positive, mostly increasing with increasing ΔP, and generally decreasing with increasing ω. Circumstances are unlikely to arise that would force a choice between GR/SS and SR/GS seal configurations, but based on K_{xx} alone, the SR/GS configuration would be preferred.

For the GR/SS seal, Fig. 12(c) shows K_{yy} to be negative, generally dropping with increasing ω, largely independent of ΔP. Figure 12(d), shows K_{yy} to be near zero or negative, generally dropping with increasing ω, and generally increasing with increasing ΔP --- the ΔP = 4 bar case providing an exception.

K_{xy}, K_{yx} Coefficients

K_{xy}, K_{yx} coefficients arise due to fluid rotation and create a destabilizing force on the seal rotor. The fluid enters the seal with an imposed rotation due to preswirl. Also, non-slip conditions at the seal and rotor fluid surfaces can either decrease or increase the seal flow circumferential velocity as the flow moves through the seal. The stator-surface forces tend to slow down fluid rotation; the rotor surface forces tend to increase fluid rotation. A GR/SS seal has decidedly more rotor surface area pushing the fluid forward in the direction of shaft rotation than the stator surface area has in retarding it. The opposite circumstance holds for an SR/GS seal. Hence, we would expect higher magnitudes for K_{xy}, K_{yx} for the GR/SS seal than for a corresponding SR/GS seal. The results of Fig. 13 are for a low inlet preswirl and shows precisely that outcome; namely, the GR/SS seal K_{xy}, K_{yx} values are approximately 2.5 times larger than the corresponding values for the SR/GS seal. In Fig. 13(a), the GR/SS values increase more-or-less linearly with increasing ω. They also generally incease with increasing ΔP. For the same conditions, Fig. 13(b) shows roughly the same outcome for the SR/GS seal except for the ΔP = 4 bar case at 4 krpm.

Generally K_{xy}, K_{yx} increase with increasing ω as expected from the PSR plots of Figs. 11(a) and 11(b). However, contrary to

expectation that K_{xy} drops with increasing ΔP in Fig.11(a), K_{xy} grows with an increase in ΔP as shown in Fig. 13(a) --- the exception arising at ΔP = 4 bars.

At ΔP = 8 bars, Fig. 14 shows the impact of changing ω and PSR on K_{xy}, K_{yx} for both seal configurations. K_{xy}, K_{yx} magnitudes increase steadily with increasing ω for both seals. Again, note that K_{xy}, K_{yx} magnitudes are roughly 2.7 times larger for the GR/SS seal than for the SR/GS seal. In Fig. 14(a), the GR/SS seal consistently shows $K_{xy} = -K_{yx}$. The K_{xy} and K_{yx} magnitudes consistently increase in moving from low to high preswirl values, but the medium preswirl result does not always lie between low and medium preswirl results.

Figure 14(b) shows (as expected) a consistent increase in K_{yx}'s magnitude as PSR increases from low to medium to high preswirl. The expected increase in K_{xy} in moving from low to medium preswirl also applies; however, the high PSR result is frequently smaller than the corresponding medium-PSR result. The results show that applying swirl brake would be more productive for the SR/GS seal than for the GR/SS seal.

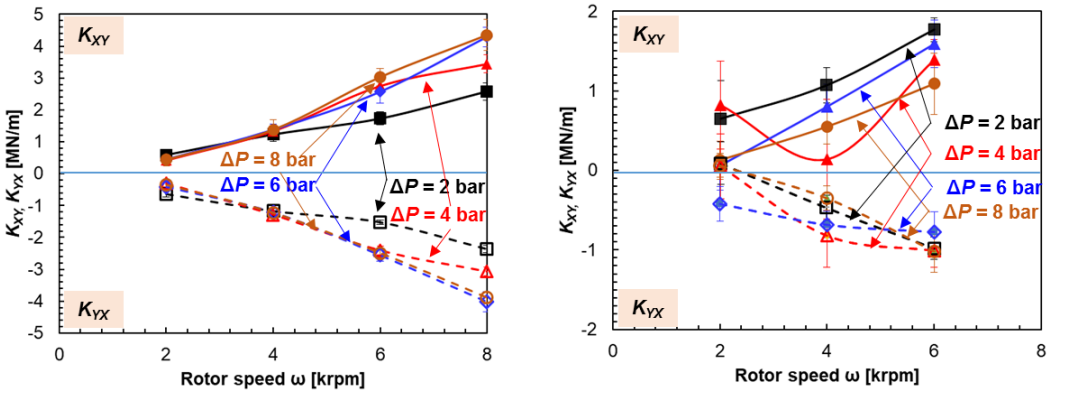

(a) GR/SS: K_{XY} and K_{YX} vs. ω (b) SR/GS: K_{XY} and K_{YX} vs. ω

Figure 13. Low inlet pre-swirl, K_{XY} and K_{YX} versus ω for both grooved seals. ΔP = 2, 4, 6, and 8 bar.

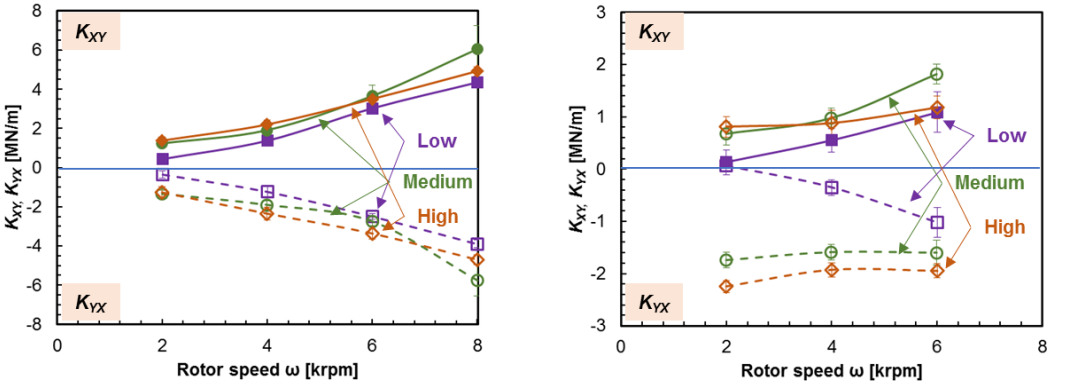

(a) GR/SS : K_{XY} and K_{YX} vs. ω (b) SR/GS: K_{XY} and K_{YX} vs. ω

Figure 14. K_{XY} and K_{YX} versus ω for both grooved seals. ΔP = 8 bar; ω = 2, 4, 6, and 8 krpm; low, medium and high inlet pre-swirl ratios.

C_{xx}, C_{yy} Coefficients

Figure 15 illustrates C_{xx}, C_{yy} versus ω for both seals for all preswirl rings at ΔP = 8 bars. The scales are the same for both seals. Figure 15(a) shows C_{xx} generally increasing with increasing ω. It is not sensitive to changing PSR inserts at 2 krpm, but becomes increasingly sensitive as ω increases. At 8 krpm, it jumps sharply in moving from the low to medium preswirl values and then drops when moving to the high preswirl. The results in Fig. 15(b) for the SR/GS seal are similar but less sensitive to changes in PSR.

The GR/SS seal results of Fig. 15(c) showing C_{yy} versus ω are quite similar to the corresponding results of Fig. 15(a) but with a reduced sensitivity to changes in PSR and ω. The C_{yy} results of Fig. 15(d) (SR/GS) is similar to Fig. 15(c) (GR/SS) except the SR/GS seal has little sensitivity to changing either ω or PSR. At the centered position, we expect C_{xx} and C_{yy} to be nearly equal. That expectation is borne out better for the GR/SS seal than for the SR/GS seal. In practical terms, one is unlikely to be asked to choose between a GR/SS seal or a SR/GS seal, but the SR/GS seal has better (higher) direct damping out to 6 krpm.

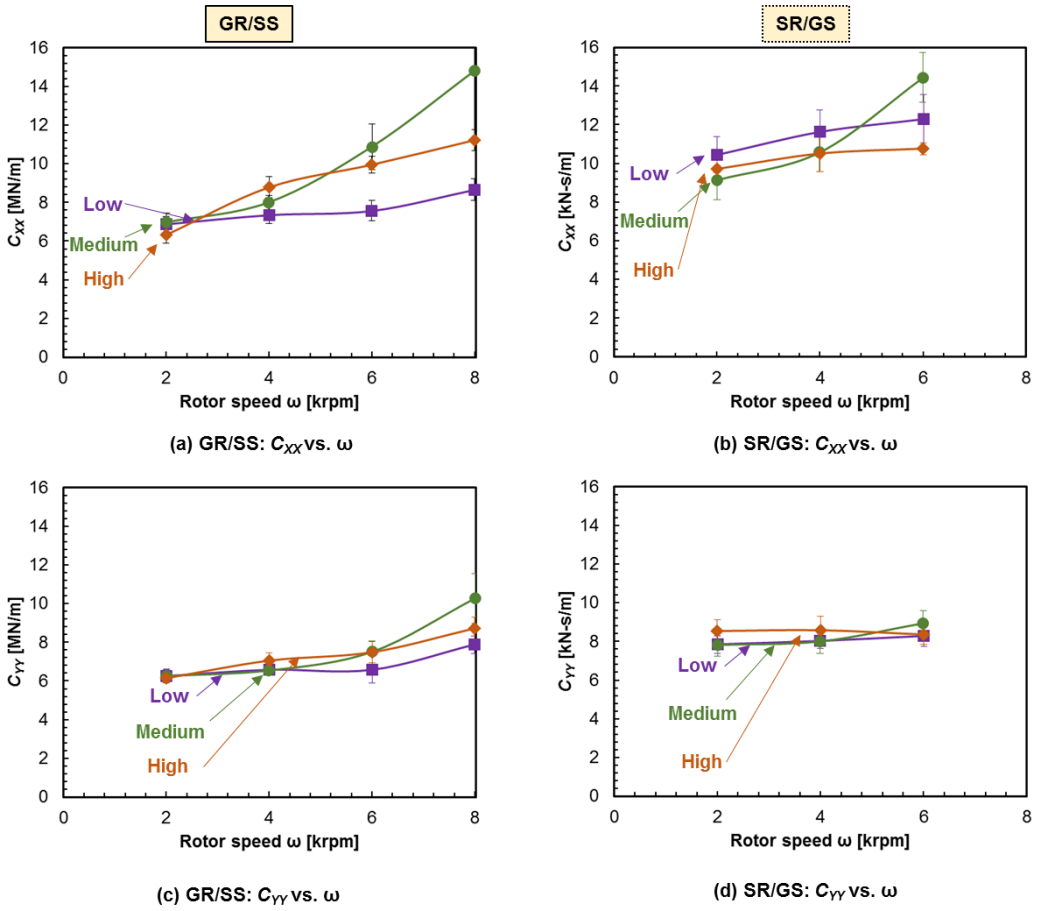

Figure 15. C_{XX} and C_{YY} versus ω for the two grooved seals. ΔP = 8 bar; low, medium and high inlet pre-swirl ratios.

C_{xy}, C_{yx} Coefficients

At ΔP = 8 bar, Fig. 16 illustrates C_{xy}, C_{yx} versus ω for all preswirl rings. Figure 16(a) applies to the GR/SS seal. Generally speaking, C_{yx} = - C_{xy}, and the coefficient magnitudes increase (as expected) more or less linearly with increasing ω. Given that these coefficients arise due to fluid rotation, one could expect a steady increase in their magnitudes with increasing preswirl, but that did not happen.

Figure 16(b) applies for the SR/GS seal. The cross-coupled damping values are roughly 2.7 times larger for the GR/SS seal than for the SR/GS seal. There is no clear pattern regarding changes in C_{xy}, C_{yx} due to changes in preswirl values. The two coefficients have generally different signs but are not equal in magnitude and opposite in sign.

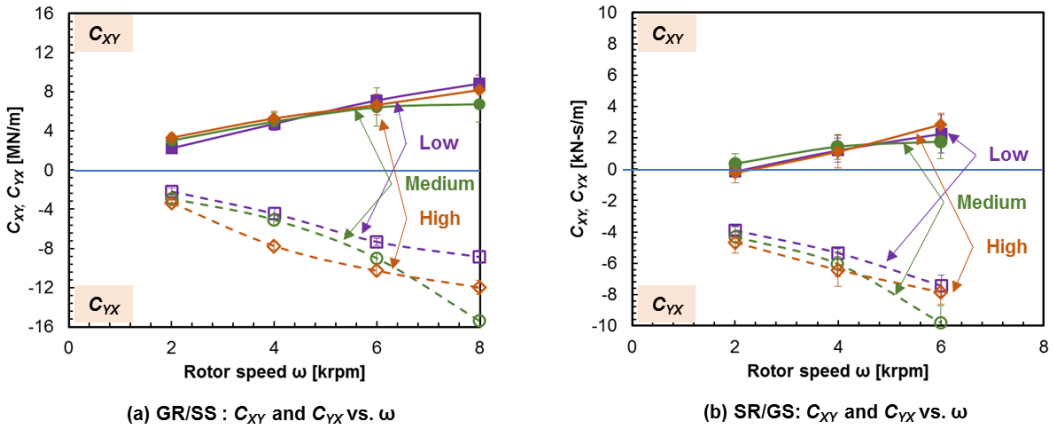

Figure 16. C_{XY} and C_{YX} versus ω. ΔP = 8 bar; ω = 2, 4, 6, 8 krpm; low, medium, and high inlet pre-swirl ratios.

M_{xx}, M_{yy} Coefficients

Figure 17 illustrates M_{xx}, M_{yy} versus ω at ΔP = 8 bar for all preswirl rings. The GR/SS seal results shown in Fig. 17(a) and 17(c) are much more sensitive to changes in ω and PSR than the corresponding results in Fig. 17(b) and 17(c) for the SR/GS seals. Generally, M_{xx}, M_{yy} values are larger for the SR/GS seals.

M_{xy}, M_{yx} Coefficients

For *smooth* seals, M_{xy}, M_{yx} arise due to fluid rotation and should be equal in magnitude and opposite in sign. The GR/SS seal coefficients in Figs. 18(a) and 18(c) for which PSR insert roughly follow that trend and would impact rotor stability. However, for the SR/GS seal in Figs. 18(b) and 18(d), M_{yx} and M_{yx} are both negative. They could impact the natural frequency of a pump but not directly impact stability. No clear pattern of behavior is seen concerning changing ΔP or ω.

The GR/SS M_{xy}, M_{yx} coefficients in Fig. 19 generally drop with increasing ω; no clear trend is displayed concerning changing PSR. For the SR/GS seal In Figs. 19(b) and 19(d), M_{xy} and M_{yx} are both negative with comparable magnitudes, implying a possible (probably small) impact on a pump's critical speed location but no impact on stability. No comparably clear trend holds for the GR/SS seal in Figs. 19(a) and 19(c).

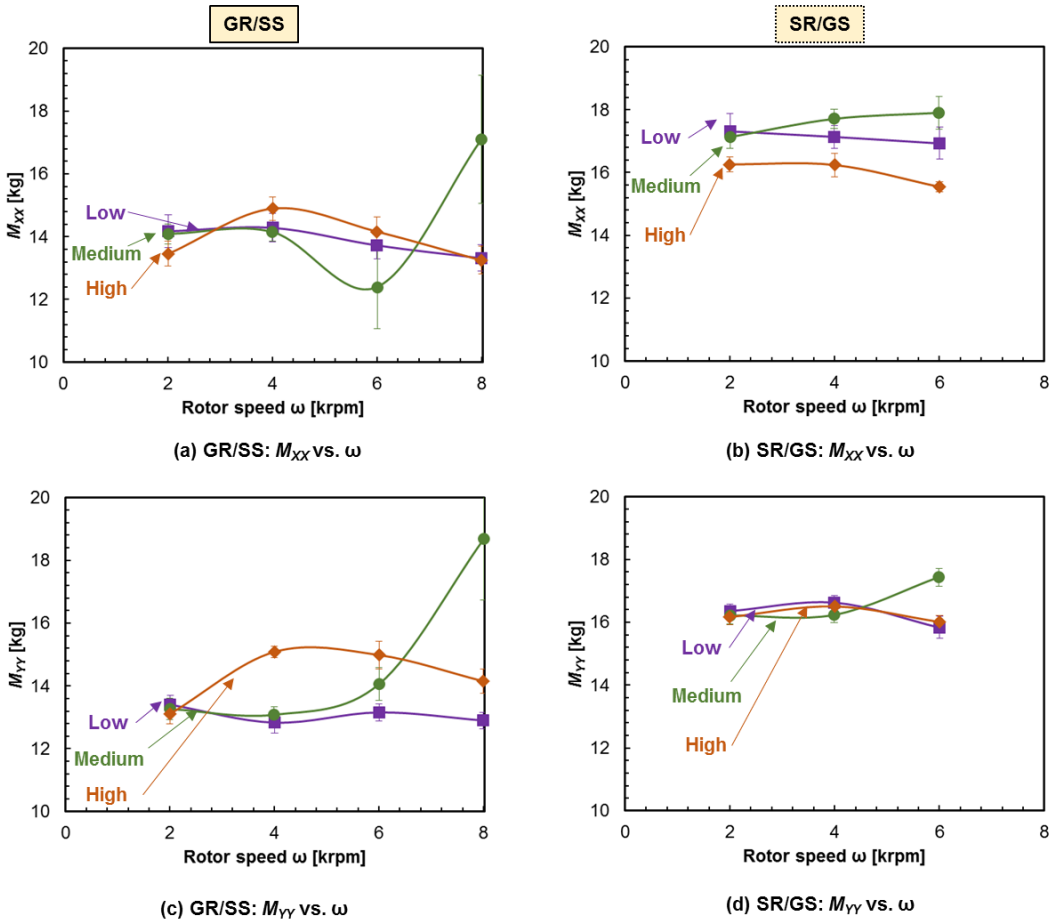

Figure 17. M_{XX} and M_{YY} versus ω . ΔP = 8 bar; ω = 2, 4, 6, 8 krpm; low, medium and high PSR inserts.

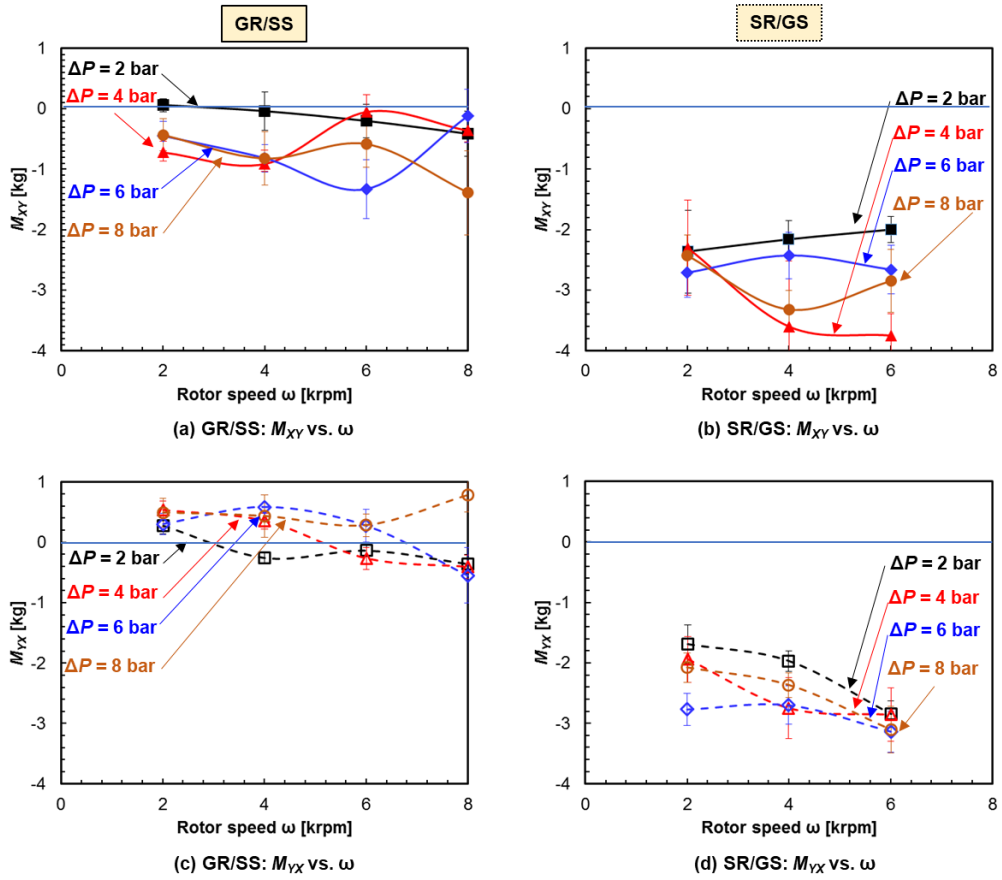

Figure 18. M_{xy} and M_{yx} versus ω, ΔP = 2, 4, 6, and 8 bar; low PSR insert.

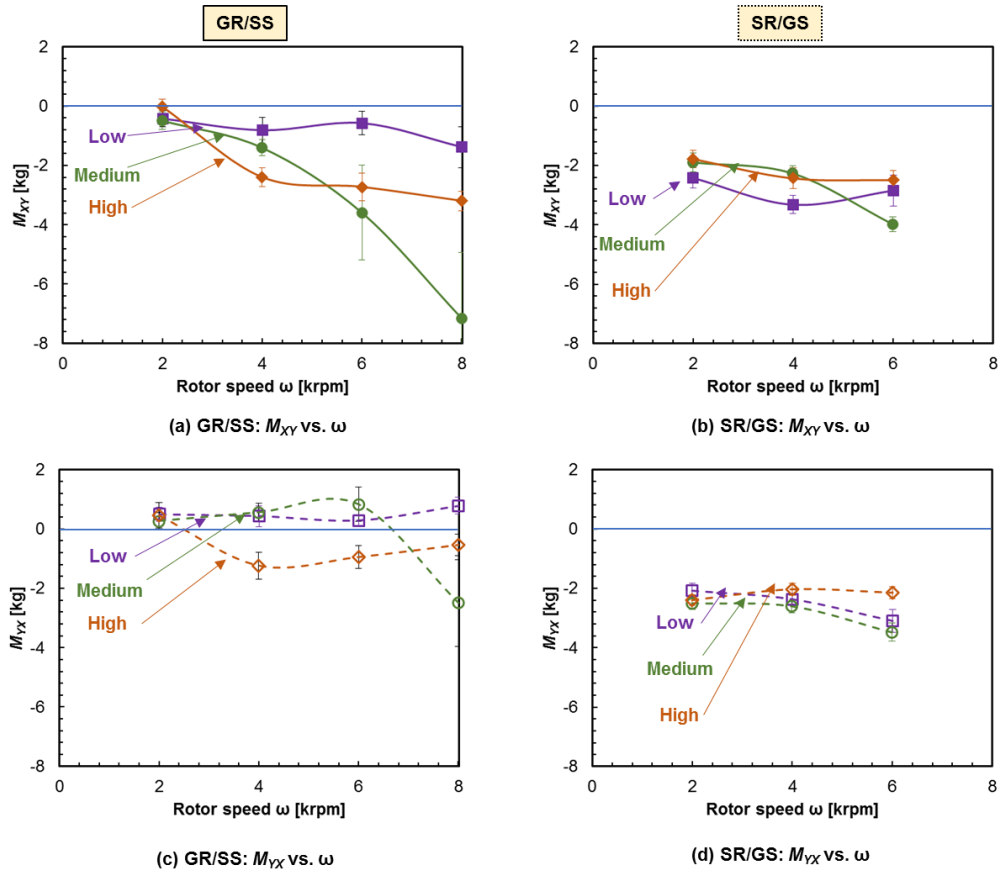

Figure 19. M_{xy} and M_{yx} versus ω at ΔP = 8 bar, ω = 2, 4, 6, 8 krpm; all PSR inserts.

Whirl Frequency Ratio

San Andrés [17] developed a whirl-frequency-ratio (WFR) definition that accounts for M_{xy} and M_{yx} terms with different signs as displayed for some of the results in Figs. 18 and 19. His definition is used here.

For the GR/SS seal, using the low PSR insert, Fig. 20(a) shows WFR versus ω over a range of ΔP values. Except at ΔP = 2 bar, WFR generally increases steadily with increasing ω. For all ΔP values, WFR reaches an asymtote of ~0.65 at ω = 6 krpm, implying that the GR/SS seal would destabilize a pump rotor at ω greater than 1/.6 = 1.67 times the rotor's 1st critical speed. This result is more destabilizing than the corrsponding WFR ~ 0.5 result for a smooth seal that would become destabilizing for ω greater than 1/.5 = 2 times the rotor's 1st critical speed. In regard to changing ΔP, no clear pattern emerges across the running speed range. Except for the ΔP = 2 bar case, WFR generally increases (becomes more destailizing) with increasing ω. This pattern is consistent with the increasing value of PSR with increasing ω shown in Fig. 11(a).

For the SR/GS seal, using the low PSR insert, Fig. 20(b) shows WFR versus ω over a range of ΔP values. WFR increases with increasing ω and generally decreases with increasing ΔP. WFR increases (less stable) with increasing fluid rotation, which explains the increase with increasing ω. For the low-preswirl insert, the fluid enters the seal with a reduced average (across the clearance) fluid velocity, and is acclerated by shear forces from the rotor as it proceeds through the seal. Increasing ΔP cause the seal leakage and axial velocity to go up, decreasing the amount of time that the rotor shear forces can acclerate the fluid's average circumferential velocity. Hence, as ΔP goes up, WFR comes down (becomes less destabilizing). Looking back at Fig. 11(b), both PSR and WFR increase with increasing ω.

In comparing Figs. 20(a) and 20(b), note that WFR is markedly smaller (more stable) for the SR/GS seal than for the GR/SS. The SR/GS seal has substantially more stationary stator surface acting to slow the average circumferential down than rotor surface trying to speed it up. The opposite situation holds for the GR/SS seal.

For the GR/SS seal, at ΔP = 8 bars, Fig. 21(a) shows WFR versus ω for all inlet preswirl inserts. At 2 and 4 krpm, WFR increases steadily (becomes more destabilizing) in moving from the low to medium to high preswirl inserts. At 6 and 8 krpm, all of the values tend to approach 0.65. The high-preswirl curve in Fig. 21(a) mirrors the ΔP = 8 bars PSR versus ω curve of Fig. 11(c). The low-preswirl curve mirrors the ΔP = 8 bars PSR versus ω curve of Fig. 11(a).

For the SR/GS seal, at ΔP = 8 bars, Fig. 21(b) shows WFR versus ω for all inlet PSR inserts. In all cases, WFR increases in moving from the low to medium to high preswirl inserts. PSR drops with increasing ω for the high and medium inserts and increases with increasing ω for the low-preswirl insert. For the 2-6 krpm speed range displayed, adding a swirl brake would always improve the SR/GS seal's stability characteristics.

Comparing WFR for the GR/SS (Fig. 21(a)) and the SR/GS (Fig. 21(b)), the SR/GS seal is always more stable --- lower WFR.

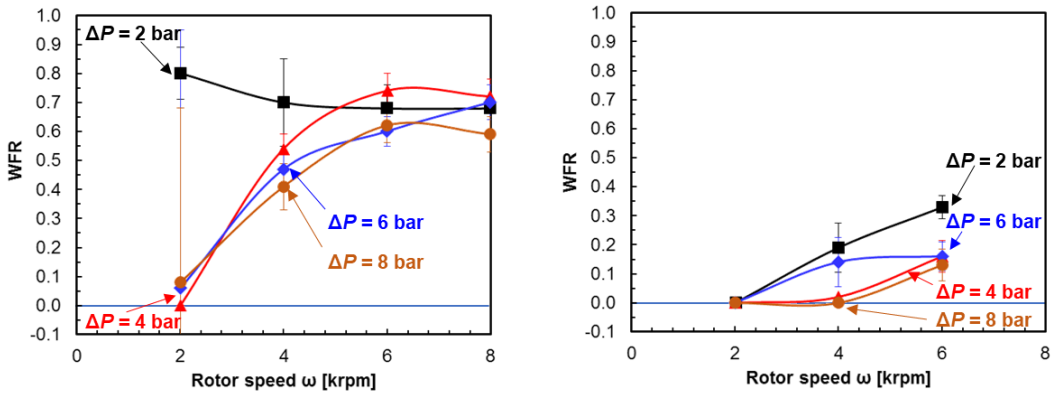

Figure 20. low PSR insert; ω = 2, 4, 6, 8 krpm. WFR versus ω for (a) GR/SS seal; ω = 2, 4, 6, 8 krpm, and (b) SR/GS seal; 2, 4, 6 krpm.

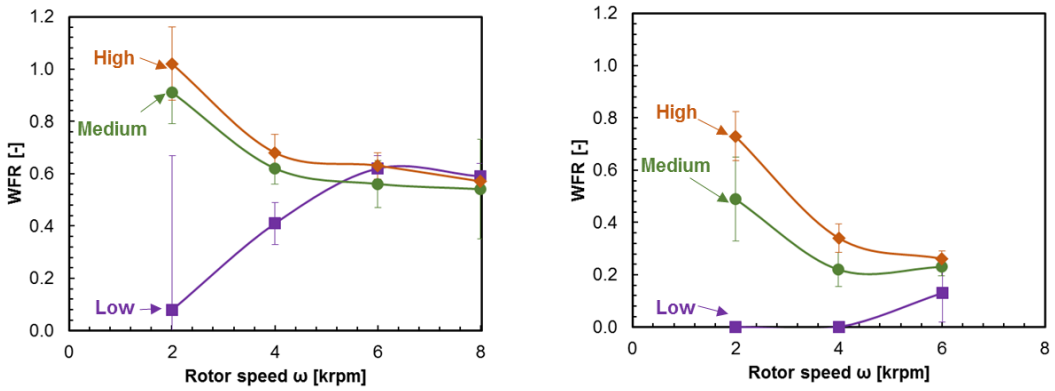

Figure 21. ΔP = 8 bar; WFR versus ω [krpm] for both seals. Low, medium and high PSR inserts.

SUMMARY, DISCUSSION, AND CONCLUSIONS

Static and rotordynamic test results are presented for a smooth-rotor/grooved-stator (SR/GS) seal and a grooved-rotor/smooth-stator (GR/SS) seal in a centered location. The GR/SS seal has the dimensions of an electrical submersible pump (ESP) interstage seal. The SR/GS seals' nominal dimensions are identical with the GR/SS seal except for the reversed groove locations. Test results are presented for a centered location and include static and rotordynamic data at speeds ω of 2, 4, 6 krpm for the SR/GS and 2, 4, 6, 8 krpm for the GR/SS seal. Both seals have axial pressure drops ΔP of 2.1, 4.1, 6.2, 8.3 bars, a length-to-diameter ratio L/D of 0.5, and a minimum design radial clearance C_r of .203 mm. They employ 15 circumferential grooves with a length G_l, and depth G_d of 1.52 mm, which are equally spaced with a land length of 1.52 mm. Three different inlet-fluid pre-rotation inserts are used upstream of the test seals to create a range of inlet preswirl ratios (PSRs).

The present test results are taken from the TAMU theses [9, 10]. Some of the results were presented in papers [7, 8] where the grooved seals' performances were compared to smooth seals, and the following conclusions were determined:

(a) Smooth seals leak more.
(b) Smooth seals have markedly larger direct stiffness and direct damping values than grooved seals.

SR/GS seals are commonly used in pumps. GR/SS seals are generally only used when the product fluid contain considerable amounts of particulates, including ESPs. Smith et al. [18] reported on a coke-crusher pump that used GR/SS seals to cope with particulates in the flow. The pump became unstable in some operating conditions. It ran at 3600 rpm, and was super-synchronously unstable, precessing at 1.3 times running speed. The pump had a back-to-back, two stage design and used unshrouded impellers. The whirl frequency of 1.3 probably arose because of both: (a) the GR/SS design, and (b) the choice of unshrouded impellers. Uchiumi et al. [19] presented rotordynamic test results for unshrouded impellers, showing them to have negligible direct damping and high levels of destabilizing cross—coupled stiffness coefficients. The problem was remedied by replacing the GR/SS design with a smooth seal. Massey [20] presents one of several case-study publications where a pump is originally unstable and is stabilized by replacing SR/GS seals with smooth seals and adding a swirl brakes.

In practical terms, a pump designer is unlikely to replace a GR/SS seal with a SR/GS seal (or the opposite swap) for improvements in either leakage or rotordynamics. Similarly, in cases where stability issues arise, improving stability by only adding a swirl brake (not swapping out grooved for smooth seals) is also unlikely. Nonetheless, in the present paper the leakage and rotordynamic properties are, for the first time, compared directly. Their comparative performance is discussed below.

Leakage

The GR/SS seal leaks about 10% more than the SR/GS seal.

Direct Stiffness

Generally, K_{xx}, K_{yy} values are small for both designs and drop with increasing ω. The GR/SS seals' K_{xx}, K_{yy} values dropped more rapidly and were negative at 6 krpm. For the SR/GS seals, K_{yy} was negative at 6 krpm but K_{xx} was still positive. With either groove design, rotordynamic instability issues are as likely to arise because of: (a) negative stiffness that pulls down a pump's critical speed, versus (b) directly destabilizing K_{xy}, K_{yx} coefficients.

Cross-Coupled Stiffness

In the same test conditions, the magnitudes of K_{xy}, K_{yx} coefficients are ~2 times larger for GR/SS seals than for the SR/GS seals --- significantly more destabilizing.

Direct Damping

Under the same conditions, the SR/GS seal has slightly more direct damping than the GR/SS seal.

Cross-Coupled Damping

These coefficients are comparable for the two designs and of secondary importance from a rotordynamics viewpoint.

Direct Virtual Mass

M_{xx}, M_{yy} coefficients are about 20% larger for the SR/GS seals, inducing lower pump critical speeds.

Cross-Coupled Virtual Mass Terms

For both seals, the terms are small compared to M_{xx}, M_{yy} values. M_{xy}, M_{yx} have the same (negative) sign for the SR/GS seal. That outcome could impact a pump's critical speed, but would not as directly impact stability. For the GR/SS seal, in some cases M_{xy}, M_{yx} have different signs and could directly impact stability.

Whirl Frequency Ratio

WFR combines the effects of (K_{xy}, K_{yx}), (C_{xx}, C_{yy}) and (M_{xy}, M_{yx}). Hence, putting aside the impact of differing values for K_{xx}, K_{yy} and M_{xx}, M_{yy} on the pump rotor's critical speed, WFR provides the best measure for comparing the stability characteristics of the two seal designs. Overall, the GR/SS seal WFR values are about three times higher than the comparable values for SR/GS seals --- much less stable.

Potential for Stability Improvements via Implementation of Swirl Brakes (Only)

The test results predict that effective swirl brakes, that could sharply drop the seal's inlet preswirl, would be helpful for the GR/SS seal out to 4 krpm and helpful for the SR/GS seal out to 6 krpm.

NOMENCLATURE

C_r	Minimum seal radial clearance [L]
C_r/R	Clearance-to-radius ratio [-]
D	Seal inner diameter [L]
L	Seal axial length [L]
$\dot{Q}$	Individual Seal volumetric leakage rate
R	Shaft radius [L]
v_{inlet}	Measured circumferential velocity at the inlet of the seal [L/T]

Greek Symbols

ϵ_0	Eccentricity ratio [-]
ΔP	Axial pressure-drop across the seal [F L^2]
ρ	Fluid density [M/L^3]
ω	Angular shaft speed [T^{-1}]
Ω	Excitation frequency [T^{-1}]

Subscripts

i	Direction of system response, $i = x, y$
j	Direction of perturbation, $j = x, y$

Abbreviations

GR/SS	Smooth rotor-circumferentially-grooved stator.
SR/GS	Smooth-Stator-circumferentially rotor.
PSR	Pre-swirl ratio, defined in Eq. (3)
WFR	Whirl frequency ratio

REFERENCES

[1] Lomakin, A., 1958, "Calculation of the Critical Number Of Revolutions and Conditions Necessary for Dynamic Stability of Rotors in High-Pressure Hydraulic Machines When Taking Into Account Forces Originating in Sealings," Journal For Power And Mechanical Engineering (In Russian), **14**, pp. 1-5.

[2] Li, Z., Fang, Z., Li, J., and Feng, Z., 2019, "Numerical Comparison of Static and Rotordynamic Characteristics for a Grooved-Stator/Smooth-Rotor and a Smooth-Stator/Grooved Rotor Liquid Annular Seals," Proceedings of the 2019 ASME Turbo Expo, Phoenix, Arizona, USA, ASME Paper No. GT2019-90781.

[3] Florjancic, S., and Mccloskey, T., 1990, "Measurement and Prediction of Full Scale Annular Seal Coefficients," Eighth International Pump Users Symposium, pp. 71–87.

[4] Kilgore, J. J., and Childs, D. W., 1990, "Rotordynamic Coefficients and Leakage Flow of Circumferentially Grooved Liquid-Seals," ASME J. Fluids Eng, **112**(3), pp. 250–256.

[5] Marquette, O., Childs, D., and Philips, S., 1997, "Theory versus Experiment for Leakage and Rotordynamic Coefficients of Circumferentially-Grooved Liquid Annular Seals with *L/D* of 0.45," Proceedings of the 1997 ASME Fluids Engineering Division Summer Meeting, Vancouver, Canada, Paper No. FEDSM97-3333, pp.22-26.

[6] Glienicke, J., 1996, "Experimental Investigation of Stiffness and Damping Coefficients of Turbine Bearings and their Application to Instability Predictions," Proceedings of the Institution of Mechanical Engineering, London, England, **181**(2), pp. 116–129.

[7] Moreland, J. A., Childs, D. and J. Bullock, 2018, "Measured Static and Rotordynamic Characteristics of a Smooth-Stator/Grooved-Rotor Liquid Annular Seal," ASME J. Fluids Eng., **140**(10), pp.101109.

[8] Childs, D., Rueda, J., and J. Bullock, 2018, "Static And Rotordynamic Characteristics of Liquid Annular Seals with a Circumferentially-Grooved Stator and Smooth Rotor Using Three Levels of Circumferential Inlet-Fluid Rotation," Proceedings of the 2018 ASME Turbo Expo, Oslo, Norway, ASME Paper No. GT2018-75325.

[9] Moreland, J.A., 2016, "Influence of Pre-Swirl and Eccentricity in Smooth Stator/Grooved Rotor Liquid Annular Seals, Measured Static and Rotordynamic Characteristics," M.S. Thesis, Mechanical Engineering Department, Texas A&M University.

[10] Torres Rueda, J.M., 2017, "Static and Rotordynamic Characteristics of Liquid Annular Seals with a Circumferentially-Grooved Stator and Smooth Rotor Using Three Levels of Circumferential Inlet-Fluid Rotation," M.S. Thesis, Mechanical Engineering Department, Texas A&M University.

[11] Childs, D., Norrbin, C., and S. Phillips, 2014, "A Lateral Rotordynamics Primer on Electric Submersible Pumps (ESPs) For Deep Subsea Applications," Proceedings of 43rd Turbomachinery and 30th Pump Users Symposia, September 23-25, Houston TX. DOI: https://doi.org/10.21423/R15K8Q.

[12] Kaul, A., 1999, "Design and Development of a Test Setup for the Experimental Determination of the Rotordynamic and Leakage Characteristics of Annular Bushing Oil Seals," M.S. Thesis, Texas A&M University.

[13] Kleuitenberg, M., 2014, "Experimentally Determine the Impact of Inactive Jacking Ports on Rotordynamic Characteristics of a Four-Pad, LBP, Tilting-Pad Journal Bearing," M.S. Thesis, Texas A&M University.

[14] Rouvas, C., and D. Childs, 1993, "A Parameter Identification Method for Rotordynamic Coefficients of A High Reynolds Number Hydrostatic Bearing," ASME, J. Vib. Acoust., **115**(3), pp. 264–270.

[15] Childs, D. W., and Hale, K., 1994, "A Test Apparatus and Facility to Identify Rotordynamic Coefficients of High-Speed Hydrostatic Bearings," ASME J. Tribol., **116**(2), pp. 337–343.

[16] Beckwith, T., Marangoni, R., And Lienhard, V.J., 2007, Mechanical Measurements, Pearson Education, Inc, Upper Saddle River, NJ.

[17] San Andres, L., 1991, "Effect of Eccentricity on the Force Response of a Hybrid Bearing," Tribol. Trans., **34**(4), pp. 537–544.

[18] Smith, D., Price, S., and Kunz, F., 1996, "Centrifugal Pump Vibration Caused by Supersynchronous Shaft Instability," Proceedings, 13th Pump Users Symposium, Turbomachinery Laboratory, Texas A&M University, pp. 47-60.

[19] Uchiumi, M., Nagao, N., Yoshida, Y,, and M. Eguchi, 2012, "Comparison of Rotordynamic Fluid Forces Between Closed Impeller and Open Impeller," Proceedings of the 2012 ASME Fluids Engineering Summer Meeting, July 8-12, Rio Grande, Puerto Rico, Paper No. FEDSM2012-72348.

[20] Massey, I., (1985), "Subsynchronous Vibration Problems in High-Speed Multistage Centrifugal Pumps," Proceedings of the 14th Turbomachinery Symposium, Turbomachinery Laboratory, Texas A&M University, pp. 11-16.

